Doping evolution of second magnetization peak and magnetic relaxation in $(Ba_{1-x}K_x)Fe_2As_2$ single crystals

Yong Liu[1,*] Lin Zhou[1], Kewei Sun[1], Warren E. Straszheim[1], Makariy A. Tanatar[1,2], Ruslan Prozorov[1,2], and Thomas A. Lograsso[1,3]

[1]*Division of Materials Sciences and Engineering, Ames Laboratory, U.S. DOE, Ames, Iowa 50011, USA*

[2]*Department of Physics and Astronomy, Iowa State University, Ames, Iowa 50011, USA*

[3]*Department of Materials Science and Engineering, Iowa State University, Ames, Iowa 50011, USA*

Magnetic hysteresis behavior was systematically studied in a series of $(Ba_{1-x}K_x)Fe_2As_2$ ($0.18 \le x \le 1$) single crystals with magnetic fields applied parallel to c axis ($H \parallel c$). Second magnetization peak (SMP) is observed in magnetization hysteresis loops (MHLs) within the doping range $0.18 \le x \le 0.38$ and $0.51 \le x \le 0.64$. Interestingly, the SMP disappears within a narrow doping range $0.4 < x < 0.5$. With increasing x approaching 0.70, the SMP shifts towards high field region, similar to the so-called "peak effect" (PE) observed in conventional superconductors. Above x=0.70, the PE is weak but still discernible untill the sample x=0.91. No PE is observed in the end member x=1. By calculating the critical current density J_c with Bean model, we find that J_c reaches maximum of 3.3×10^6 A/cm^2 at x=0.26 under the same reduced temperature T/T_c=0.2 and H=0.5 T when comparing the doping dependent J_c for all the samples. The doping x=0.26 corresponds to the critical doping above which the antiferromagnetic (AFM) order is completely

* Corresponding author. Email address: yliu@ameslab.gov

suppressed and materials becomes tetragonal structure in the $(Ba_{1-x}K_x)Fe_2As_2$ phase diagram. Our previous optical studies have revealed that structural orthorhombic domains are clearly present for $x<0.26$, which are most likely responsible for the maximum of J_c. All samples within the doping range $0.18\leq x\leq 0.70$ show the paramagnetic Meissner effect (PME) in the temperature dependent magnetization measurements except the samples $x=0.43$ and 0.46 where no SMP is observed as well. The dopings 0.43 and 0.46 are very close to 1144 system *Ae*AFe_4As_4 (*Ae*=Ca, Sr; *A*=K, Rb, Cs), where *Ae* and *A* do not occupy crystallographically equivalent sites because of the large differences between their ionic radii and the *Ae* and *A* layers are inserted alternately between the Fe_2As_2 layers in the *c*-axis direction [Iyo et al., J. Am. Chem. Soc. **138**, 3410 (2016).] Assuming the similar structure forms in $(Ba_{1-x}K_x)Fe_2As_2$ compounds within the doping range $0.4<x<0.5$, the SMP apparently disappears because of a less disordered structure. We find that the decay of magnetization nearly follows power-law time dependence, while the creep activation barrier U can be described by the logarithmically dependent relation on the critical current J. We propose two types of pinning sources that dominate the different doping regimes in the samples, i.e., domain walls in the underdoped regime and the spatial fluctuations of dopant atoms in the overdoped regime.

PACS number(s): 74.70.Xa, 74.25.Wx, 74.25.Sv

I. INTRODUCTION

The studies of vortex dynamics revealed many interesting phenomena in the iron pnictide superconductors. Because of the availability of large and high–quality single crystals, most of researches have been done on 122-type superconductors with $ThCr_2Si_2$ structure. Similar to high T_c cuprate supercondcutors, a pronounced second magnetization peak (SMP) was observed in magnetization hysteresis loops (MHLs) of $(Ba_{1-x}K_x)Fe_2As_2$ [1-6], $Ba(Fe_{1-x}Co_x)_2As_2$ [3,6,7-13], $BaFe_2(As_{1-x}P_x)_2$ [6,14-15]. One of striking features that that distinguish iron pnictide supercondcutors from high T_c cuprate supercondcutors is the observation of strongly disordered vortex structure in iron pnictide supercondcutors by Bitter decoration [16-22], scanning tunneling microscopy (STM) [23-24], magnetic force microscopy (MFM) [25], small-angle neutron scattering (SANS) measurements [17-18,26-27]. Although long-range ordered vortex lattice (VL) was not observed yet, the so-called Bragg glass may exisit, which is a glass but nearly as ordered as a perfect crystal. An ordered vortex structure was observed in an area of 130×50 nm^2 in optimally doped $Ba_{0.6}K_{0.4}Fe_2As_2$ by STM measurement [28]. With a large $Ba_{0.64}K_{0.36}Fe_2As_2$ single crystal, SANS measurement observed Bragg peaks corresponding to a long-range orientationally ordered triangular lattice below H=0.75 T. With increasing magnetic field above 0.75 T, diffraction spots smeared and gave the characteristic pattern of circles from a polycrystalline structure, which was interpreted as a vortex order–disorder transition associated with the the appearance of SMP in MHLs [29]. In optimally doped $BaFe_2(As_{0.67}P_{0.33})_2$ single crystals, hexagonal VL was formed in the field range from 1 to 16 T revealved by SANS measurement, and no symmetry changes in the VL were observed [30]. In KFe_2As_2 single crystals, a well-ordered hexagonal VL was observed by SANS measurement, with no symmetry transitions up to high fields [31-32].

The disordered VL structure is directly related to a random distribution of pinning potential, implying the pinning mechanisms in iron pnictide superconductors. A pinning potential, U_0, as high as 10^4 K, was reported in a $Ba_{0.72}K_{0.28}Fe_2As_2$ crystal [33]. The vortex pinning was ascribed to a dense vortex pinning nanostructure, perhaps resulting from an inhomogeneous distribution of cobalt ions in $Ba(Fe_{0.9}Co_{0.1})_2As_2$ single crystal [8]. Van der Beek *et al*. suggested the existence of two types of pinning sources: (i) Strong pinning resulting from the heterogenity on the scale of a few dozen to 100 nm; (ii) Weak collective pinning resulting from a disorder at the atomic scale induced by the dopant atoms [34-36]. Through an analysis of the vortex interaction energy and pinning force distributions extracted from Bitter decoration images for $Ba(Fe_{1-x}Co_x)_2As_2$ and $BaFe_2(As_{1-x}P_x)_2$ single crystals, the disordered VL was suggested to be resulted from an inhomogeneous distribution of the dopant atomes on the scale of several dozen to several hundred nanometers [21-22]. Furthermore, it was suggested that the disordered VL is established at a high freezing temperature T_f at $T_f = 0.95T_c$ for $Ba(Fe_{1-x}Co_x)_2As_2$ and $T_f \approx 0.87T_c$ for $BaFe_2(As_{1-x}P_x)_2$ [21-22].

In this study, high quality $(Ba_{1-x}K_x)Fe_2As_2$ single crystals were measured as a function of magnetic field H, time t, and temperature T in a wide doping range $0.18 \leq x \leq 1$. We find that the SMP is absent in the samples x=0.43 and 0.46. Furthermore, these samples show reversible magnetization in a broad temperature range for the zero field cooling (ZFC) and field cooling (FC) branches in the temperature-dependent magnetization measurements, whereas the paramagnetic Meissner effect (PME) is observed in other samples. The decay of magnetization nearly follows a power-law time dependence in $(Ba_{1-x}K_x)Fe_2As_2$ single crystals. The logarithmic dependence of the activation energy U on the critical current J is deduced. We propose two types of pinning sources that dominate the different doping regimes in the samples.

II. Experimental details

The details of growth of $(Ba_{1-x}K_x)Fe_2As_2$ single crystals can be found in Refs. 37 and 38. For magnetization measurements, the large crystals were cut into small plates with typical dimensions of $3 \times 2 \times 0.02$ mm^3 using razor blade. It should be pointed out that the superconducting transition temperature T_c spans several Kelvins for the measured crystals cleaved from one large crystal, which manifests a macro inhomogeneity in the large crystals. Only those crystals showing sharp transition were selected for our study. All the observed features and physical properties are reproducible through the measurements on eighty samples.

Magnetization measurements were performed on Vibrating Sample Magnetometer (VSM) in Physical Property Measurement System (PPMS, Quantum Design). The data were collected after cooling the sample from above T_c to the desired temperature under zero magnetic field or with an application of magnetic field, termed as ZFC and FC, respectively. The MHLs were measured at different temperatures in ZFC procedure. The magnetic field H was applied parallel to the c axis ($H \parallel c$), i.e., perpendicular to the surface of the thin plates. The magnetic field H was ramped at a sweep rate of 1×10^{-3} T/sec between -9 T and $+9$ T.

For magnetic relaxation measurements, the sample was cooled down to the measurement temperature in ZFC procedure. The magnetic field H was then increased to the desired value at a rate of 1×10^{-3} T/sec. After the field was ramped to the desired field, the superconducting coil was changed to persistent mode and the time dependence of magnetization, M vs t curve, was immediately recorded over a period of 1×10^{4} sec.

Temperature dependent magnetization data were recorded in both ZFC and FC procedures. The sample was cooled down to 2 K from above T_c in zero applied magnetic field, and $M(T)$ data were then collected on warming at 1 K/min under an applied field H. The sample was cooled

down to 2 K under the same field, and then the FC data were collected on warming at same ramping rate.

The crystal structure analysis by X-ray diffraction can be found in our previous reports [38-39]. Composition of the crystals was determined by using wavelength dispersion x-ray spectroscopy (WDS) of electron microprobe analysis.

Transmission electron microscope (TEM) samples were prepared using an FEI Helios Focused Ion Beam (FIB). TEM characterization was performed on a probe aberration-corrected scanning transmission electron microscope (AC-STEM) (FEI Titan Themis) with a Super-X energy dispersive X-ray spectroscopy (EDS) detector.

III. Results and discussion

A. Second magnetization peak and scaling relation of pinning force density

Figure 1 shows the superconducting transition curves of $(Ba_{1-x}K_x)Fe_2As_2$ (x=0.18, 0.38, 0.43, 0.51, 0.70, and 0.91) single crystals and their MHLs at selected temperatures in the configuration of $H \parallel c$. The sharp superconducting transitions demonstrate high quality of the crystals used in this study. The MHLs of the samples $0.18 \leq x \leq 0.70$ display a rather symmetric shape for the upper (M^+) and lower (M^-) branches, which suggests dominant bulk pinning in these samples. All of MHLs exhibit a sharp central peak at around H=0 T. With increasing field, magnetization curves pass through a minimum at a field H_{on}. Above H_{on}, magnetization continuously increases and reaches maximum at a field H_{sp}, so-called SMP named after the low field peak at H=0. With further increasing field, magnetization starts to decrease. The irreversible magnetization ends at an irreversibility field H_{irr}, where the upper and lower branches of the MHLs merge together with increasing field. Interestingly, SMP disappears in the samples x=0.43 and 0.46. It should be pointed out that Song *et al*. had reported doping dependence of critical

current density J_c of $(Ba_{1-x}K_x)Fe_2As_2$ single crystals within the doping range $0.23 \leq x \leq 0.52$, which was determined by the MHL measurements [5-6]. In Song *et al*.'s samples, SMP is absent in the doping range $0.36 \leq x \leq 0.50$ [5-6]. The two results are qualitatively consistent with each other. The similar results obtained in two independent works strongly suggest that the absence of SMP is intrinsic phenomenon in $(Ba_{1-x}K_x)Fe_2As_2$ system. We find that the SMP reappears in the MHLs for the samples $0.51 \leq x \leq 0.64$. For the samples in the doping range $0.70 \leq x \leq 0.91$, the SMP is observed at high field region close to H_{irr}. And the asymmetric MHLs suggest that the surface pinning and geometrical barrier dominate instead of bulk pinning. For the pure KFe_2As_2 sample, there is no SMP observed in the asymmetric MHLs [37].

In our underdoped, optimally doped samples $0.18 \leq x \leq 0.38$ and overdoped samples $0.51 \leq x \leq 0.64$, the SMP is featured as a broad peak positioned in the intermediate field away from H_{c2}. It is necessary to distinguish the high field peak observed in the example x=0.70 from the SMP observed in lower doping samples. In conventional superconductors, the SMP is positioned in the vicinity of the upper critical field H_{c2} and the MHLs exhibit a narrow width in a wide field region befor the SMP shows up, termed as peak effect (PE); see an example of Nb_3Sn superconductor in Reference 40. It is generally accepted that PE in conventional superconductors signals a rapid softening of the elastic moduli of the VL as H_{c2} is approached, which in turn can get distorted vortices pinned more strongly by pinning centers and lead to a sharp rise in the critical current [41]. Interestingly, the transformation from SMP to PE was also observed in $BaFe_2(As_{1-x}P_x)_2$ system with increasing P doping x [14].

In order to explore the vortex pinning mechanisms, the critical current density J_c has been calculated from the width of the MHLs using the Bean model $J_c = 20\Delta M/[w(1 - w/3l)]$, where ΔM is in unit of emu/cm^3, l is the length and w is the width of the sample ($w<l$) [42].

Figure 2 shows the double-logarithmic plots of field dependence of J_c for the samples x=0.18, 0.24, 0.28, 0.32, 0.38, 0.43, 0.46, 0.51, 0.64, 0.70, 0.77, and 0.91. For the samples x=0.24, 0.28, 0.32, and 0.38, J_c decreases slightly with increasing field at the low field regiome (H<0.5 T), leading to the formation of a plateau. With further increasing field, J_c follows a power-law decrease $J_c \propto H^{-n}$. The power-law dependence terminates at the onset position (H_{on}) of the SMP. The exponent n varies from 0.44 to 0.63 with increasing doping. Van der Beek *et al*. suggested that the critical current density J_c in iron pnictides consists of two parts: (i) Strong pinning gives rise to low field peak (the plateau) and power law dependence of $J_c(H)$, which is resulted from the spatial variations of the average dopant atom density on a scale of dozens of nanometers; (ii) Weak collective pinning is field-independent and leads to the formation of SMP, where the dopant atom were treated as points defects [34-36]. For the samples x=0.43 and 0.46, J_c continuously decreases without rising again. For the samples x=0.51 and 0.64, the SMP reappears. With x exceeding 0.70, the SMP changes to PE. In heavily K doped sample x=0.91, the PE is discernible but very weak. We notice that the exponent n becomes large with increasing doping, up to 0.78 in the sample x=0.91. Starting from the sample x=0.43, the plateau shrinks and it eventually vanishes above x=0.64. These features suggest that vortex pinning is strong in underdoped regime but becomes weak in overdoped regime, which implies different pinning mechanisms in these doping regimes.

The pinning force density F_p is equal to the critical value of the Lorentz force $F_p = J_c \times H$. There is a maximum F_p^{max} in the plot of F_p vs H. For type II superconductors, it was shown that the normalized pinning force $f = F_p/F_p^{max}$ as a function of reduced field $h = H/H_{c2}$ obeys a scaling relation, i.e. $f = Ah^p(1-h)^q$, where A is prefactor, p and q are the exponents that describe the actual pinning mechanism [43-45]. If single vortex pinning mechanism dominates,

the plots of f vs h at different temperatures will fall on a single curve for a given sample. The peak position h as well as the extracted fitting parameters p and q has been used to judge the types of pinning centers in iron pnictide superconductors [1,3,5,6,8,14]. Here, the parameter H_{c2} has been replaced by the irreversibility field H_{irr}. In this study, H_{irr} is defined with the criterion J_c=10 A/cm^2, where the hysteresis width ΔM decreases to a noise level.

Figure 3 shows the plots of the normalized pinning force F_p/F_p^{max} vs the reduced applied magnetic field $h=H/H_{irr}$ for the samples x=0.18, 0.24, 0.38, 0.51, 0.64, and 0.70. For the sample x=0.18, the peak position gradually shifts from 0.34 at T=3 K to 0.13 at T=9 K. For the sample x=0.24, h values shift from 0.30 at T=21 K to 0.21 at T=25.5 K. It can be seen that h values of the sample x=0.18 show a large shift compared to the sample x=0.24 in the same temperature window ΔT~4 K below T_c. The large shift of peak position in the underdoped samples sould be caused by the coexistence of the antiferromagnetic (AFM) ordered pahse and superconducting phase. In stead of plotting F_p/F_p^{max} vs $h=H/H_{irr}$, one can replace H_{irr} by H_{max}, where F_p^{max} reaches maximum [46-47]. We find that the plots of F_p/F_p^{max} vs $h=H/H_{max}$ still can be scaled to a single curve up to H_{max} for the samples x=0.18 and 0.24 (not shown in the paper). Usually, if only one pinning mechanism operates at all temperatures and fields, the pinning force F_p can be scaled on one curve. For the optimally doped samples x=0.32 and 0.38, the curves overlap well in the temperature window ΔT=2 K below T_c. The peaks are located at h=0.44 and 0.48, respectively. In a previous study, the peak positions are found at h~0.39, 0.46 and 0.56 for x=0.23, 0.30, and 0.33 in $(Ba_{1-x}K_x)Fe_2As_2$ single crystals, respectively, where the authors defined irreversibility field H_{irr} by a criterion of J_c<100 A/cm^2 [6]. A small H_{irr} will lead to a large $h=H/H_{irr}$ when ploting the scaling relation F_p/F_p^{max} vs $h=H/H_{irr}$. Both studies demonstrate that the peak positions shift from low to high h with increasing doping x. For the overdoped samples

x=0.51, h values fluctuate between 0.32<h<0.37 in a temperature window ΔT=3 K below T_c. For the samples x=0.64, we can see that the peak shifts towards low h region with increasing temperature. For the sample x=0.70, the PE is observed and h reaches 0.9 at T=12 K.

In Fig. 4(a), J_c are plotted against reduced temperature $t = T/T_c$ at a fixed field H=0.5 T for all the samples x=0.18, 0.22, 0.24, 0.26, 0.28, 0.32, 0.38, 0.43, 0.46, 0.51, 0.64, 0.70, 0.77, and 0.91. Figure 4(b) shows the doping dependent J_c at t=0.20, 0.52 and 0.80. It can be seen that J_c reach maximum at around x=0.26. This doping is exactly located at the boundary of two doping regimes in $(Ba_{1-x}K_x)Fe_2As_2$ phase diagram, where AFM transition line coupled with tetragonal to orthorhombic structure transition terminates [48-49]. The similar feature had been observed in $Ba(Fe_{1-x}Co_x)_2As_2$, where the presence of fine orthorhombic structure domains leads to the J_c maximum [10]. The orthorhombic structure domains have been directly observed in the parent compounds and underdoped samples by using polarized light microscopy [10,50-52]. In the previous studies on $(Ba_{1-x}K_x)Fe_2As_2$, high J_c were observed between $0.25 \leq x \leq 0.30$, and J_c exceed 10^5A/cm^2 at T=25K and H=6 T for x=0.30 [5-6]. To identify the origin of strong pinning at the boundary is the key to understand the pinning mechanisms and formation of SMP in $(Ba_{1-x}K_x)Fe_2As_2$ single crystals.

B. Microstructural features

The relation between microstructure, the properties of the vortex lattice, and critical currents has been the heart of the matter on the study of vortex dynamics [45]. The defects in the crystals are thought to have a strong infiuence on the pinning behavior and the shape of the magnetization curve. Compared to the intensive studies on the magnetic properties, only a few works have been done on the microstructures of iron pnictide superconductors. The structure domains in the parent compounds AFe_2As_2 (A=Sr and Ca) had been analyzed by TEM from room

temperature down to 20 K [53]. High-resolution transmission electron microscopy (HRTEM) analysis of a $Ba_{0.72}K_{0.28}Fe_2As_2$ crystal indicates no noticeable crystal defects that can act as pinning centers [33]. Defects with a size of 5–10 nm, possibly secondary phase precipitates, were observed in single crystalline $PrFeAsO_{1-y}$ [34]. It was found that $Ba(Fe_{1-x}Co_x)_2As_2$ thin films can accept a very high density of pins (15–20 vol%) without T_c suppression [54]. The vertically aligned, self-assembled pins were clarified as $BaFeO_2$ nanorods and nanoparticles in a diameter of 4–5 nm. The oxygen could be introduced when synthesizing the targets [54]. In order to explore the pinning sources in $(Ba_{1-x}K_x)Fe_2As_2$ single crystals, we performed TEM measurements on the samples x=0.38 and 0.46.

Figure 5 shows TEM results for samples x=0.38 and 0.46. The former is characteristic of the SMP, whereas the latter does not show the SMP. High resolution high-angle-annular-dark-field (HAADF) scanning transmission electron microscopy (STEM) images of sample x=0.38 along [001] and [100] zone axis are shown in Figs. 5(a) and 5(b), which demonstrate relatively high crystalline quality. A needle-like inclusion or precipitate is observed in the cross section as shown in the inset low-magnification STEM image in Fig. 5(b). This needle-like defect is nearly 500 nm long. The thickness (along c axis) of the needle-like defect is around 15 nm. Composition analysis reveals that the needle-like defect is As rich. Moreover, dislocations are observed in a low-magnification TEM image, as shown in Fig. 5(c).

Figure 5(d) shows HR-STEM image of sample x=0.46 along [001] zone axis. No defects were observed. The HR-STEM image clearly illustrates the alternating Ba/K and FeAs layers along c axis, which reveals a perfect crystallization of the studied sample. Figures 5(e)-5(h) show the elemental mapping of the sample, which evidences the homogeneous distribution of four elements inside.

C. Magnetic relaxation

Dynamic properties of the flux motion are investigated through the magnetic relaxation measurements on $(Ba_{1-x}K_x)Fe_2As_2$ (x=0.24, 0.32, and 0.43) single crystals. In Figs. 6(a) and 6(b), we show the double-logarithmic plots of $|M|$ vs t at different fields and at T=20 K for the sample x=0.24. As can be seen, $\ln|M|$ follows a linear dependence on $\ln t$ after the first two minutes. Figure 6(c) shows the MHL together with the magnetic relaxation data shown in Figs. 6(a) and 6(b), both measured at T=20 K. One can see that the SMP shifts from 2.7 T to 2 T after 1×10^4 sec. The relaxation rate S has been defined as the logarithmic time derivative of the magnetization $S = -d\ln|M|/d\ln t$ [55]. It is found that S shows a minimum at S_{min}=1.5 T. At H=9 T, magnetization rapidly decreases to its equilibrium value. Figure 6(d) shows the plots of $-T\ln|dM/dt|$ against M, which equals an activation energy U vs J relation. The slope of the curves changes at H=2 T. The analysis of field dependent relaxation data reveals a crossover of relaxation dynamics with increasing field across the SMP. The similar results had been reported in $YBa_2Cu_3O_{7-\delta}$ [56], $Ba(Fe_{0.93}Co_{0.07})_2As_2$ [9], and $Ba_{0.72}K_{0.28}Fe_2As_2$ [4], which had been interpreted as a crossover from elastic to plastic creep [4,9,56]. In the field range $H<H_{sp}$, the vortex pinning is mainly determined by the collective pinning resulted from weak point defects. The activation energy U increases with field for elastic creep, while it decreases with field for plastic creep. The creep is governed by the mechanism that has a lower potential. As field exceeds H_{sp}, the plastic creep dominates and vortices are primarily pinned by extended defects such as dislocations [56,57]. Interestingly, the relaxation rate $S(H)$ are featureless over the field range associated with the SMP in $BaFe_{1.82}Ni_{0.18}As_2$ with T_c=8 K [58].

Figure 7(a) shows the magnetization decay data collected at different temperatures and at H=0.5 T. The relaxation rate S was calculated and shown in Fig. 7(b). One can see that S does not

show a monotonic change with varying temperature. It reaches a maximum at around T=10 K, and then gradually decreases with further increasing temperature. The broad peak in $S(T)$ curves was also observed in $Ba(Fe_{1-x}Co_x)_2As_2$ single crystals with an applied field samller than the SMP field [9,12].

It is well know that the logarithmic time decay of magnetization can be interpreted within the framework of the Anderson-Kim flux-creep model, where the activation energy U is linearly dependent on current density J [55,59] For the non-logarithmic decay observed in high T_c superconductors, the collective pinning theory was proposed. Feigel'man *et al*. [60-61] considered collective pinning by weak disorder caused by a random distribution of weak defects and showed that the activation energy exhibits a power law dependence on the current density,

$$U(J) = U_0(J_c/J)^{\mu}. \quad (1)$$

Equation (1) was often modified into its interpolation form

$$U(J) = U_0[(J_c/J)^{\mu} - 1]. \quad (2)$$

Meanwhile, the magnetization decay was usually described by the interpolation formula [60,62-63],

$$J(T,t) = J_c\left[1 + \frac{\mu kT}{U_0}\ln\left(\frac{t}{t_0}\right)\right]^{-1/\mu}, \quad (3)$$

where J_c is the critical current density at which the flux creep activation barrier U vanishes, and t_0 is a microscopic time scale. In the collective creep model the exponent μ depends on the dimensionality of the system and the field and current regime. For the three-dimensional case, at low temperatures and moderate magnetic fields but relatively high currents, single vortex creep is described with μ=1/7. In the single vortex creep limit, i.e. $\mu \rightarrow 0$, the magnetization decay can be described by the power law [64]

$$J(t) = J_c(t/t_0)^{-T/U_0}. \quad (4)$$

By assuming the creep activation barrier U grows logarithmically with decreasing current J

$$U(J) = U_0 \ln(J_c/J), \tag{5}$$

Vinokur *et al*. proposed an exact solution describing flux creep in high T_c superconductors and predicted that $\ln M(t)$ exhibits a linear dependence upon $\ln t$ [64]. The logarithmic J dependence provides a good approximation for the creep activation barrier in the single-vortex creep regime.

Since we observed that the magnetization M follows the power law dependence on time t, it is expected that $U(J)$ also follows Eq. (5) in $(Ba_{1-x}K_x)Fe_2As_2$ single crystals. The method proposed by Maley *et al*. [65] was frequently used to determine the form of the temperature dependence of the activation energy U. Briefly, magnetic relaxation in superconductors is based on an Arrhenius rate equation $dM/dt \propto \exp(-U/k_BT)$, where U is effective activation energy. A rearrangement leads to

$$U = -k_BT\left[\ln\left(\frac{dM}{dt}\right) - C\right]. \tag{6}$$

Here C is a temperature-independent constant, which is used as a fitting parameter. The determination of parameter C requires that U is a continuous and smooth function of J. Since M is proportional to the superconducting current density, J, the activation energy U is usually plotted in the form of U vs M. For the sample x=0.24, the parameter C=40 yields a continuous and smooth curve, as shown in Fig. 7(c). In the previous studies, the parameters C=27 and 14 had been used in $Ba_{0.72}K_{0.28}Fe_2As_2$ [4] and $BaFe_{1.82}Ni_{0.18}As_2$ [58] single crystals, respectively. In order to get the smooth $U(M)$ curves, the activation energy U had been modified by using a scaling function $g(T/T_c) = [1 - (T/T_c)^{1.5}]$ [4,58]. In this work, the parameter C=40 works well and all the segments collected within a broad temperature range can collapse into a single curve. As shown in Fig. 7(c), $U(J)$ relation can be well described by Eq. (5). It should be pointed out that Konczykowski *et al*. found that the $U(J)$ relation in their $Ba_{0.6}K_{0.4}Fe_2As_2$ single crystals

follows Eq. (1) with μ~0.8 [66].

Figures 8(a) and 8(b) show the MHLs together with relaxation data obtained in the sample x=0.32 at T=20 K and 33 K, respectively. In Figure 8(a), MHL shows an onset peak at H_{on}, where the magnetization passes through the minimum and rapidly increases. This onset peak shifts towards low field region and vanishes with increasing temperature. It already disappears in the MHL measured at T=33 K. With increasing field, the relaxation rate S monotonously reduces but shows a kink at the field close to H_{on}. At T=33 K, the relaxation rate S passes through a minimum at H=2 T and rapidly increases, similar to those observed in the sample x=0.24. The multiple magnetization peak feature is widely observed in the doping range $0.32 \leq x \leq 0.38$ and $0.51 \leq x \leq 0.70$. Remember that the SMP disappears in the samples x=0.43 and 0.46. The observation of multiple magnetization peaks was first reported by Shen *et al*. in a $Ba_{0.6}K_{0.4}Fe_2As_2$ single crystal [67]. It should be pointed out that the similar onset peak was observed and well characterized in detwinned $YBa_2Cu_3O_{7-\delta}$ crystals [68-70]. It was suggested that onset peak corresponds to a disorder-induced transition from a relatively ordered Bragg glass to a highly disordered vortex glass [57,68-70].

Figure 8(c) shows the temperature dependence of S at a fixed field H=0.5 T. Again, one can see that S increases first and reach a maximum at T=12 K. Figure 8(d) shows the logarithmically dependent $U(J)$ relation described by the Eq. (5). For the sample x=0.32, the usuage of parameter C=40 also yields a smooth $U(J)$ curve.

Figures 9(a) and 9(b) show the double-logarithmic plots of time dependence of magnetization for the sample x=0.43 at different temperatures at H=0.5 T and different fields at T=20 K, respectively. Below T=28 K, M follows the power-law dependence on t, as shown in Fig. 9(a). For the field dependent behavior, M shows a very fast relaxation even when we

collected data at T=20 K far below T_c=38.4 K. Figures 9(c) shows a monotonic change and rapid increase of S with increasing field. Above H=3 T, M rapidly relaxes to its equilibrium value, leading to large and fluctuating S. Obviously, the pinning is very weak in the sample. The temperature dependence of S at H=0.5 T is shown in Fig. 9(d). One can see that S still shows a broad peak between $5<T<8$ K, and then increases quickly above T=15 K. Figure 9(e) shows the activation energy U also follows a logarithmic dependence on critical current J. All the segments collapse into single curve by choosing parameter C=36, which is slightly smaller than 40 used for the sample x=0.24 and 0.32. To compare among three samples x=0.24, 0.32, and 0.43, the fitting parameters with Eq. (5) are summarized in Table I.

D. Paramagnetic Meissner effect

Figure 10 shows the temperature dependence of magnetization for the samples x=0.24, 0.32, 0.43, and 0.64. The FC data are flat curves, while ZFC curves bend down to low temperatures. The insets show the superconducting transition curves in the vicinity of T_c. One can see that ZFC and FC curves show a very short reversible magnetization below T_c for the samples x=0.24, 0.32, and 0.64. With further cooling, ZFC and FC curves separate at a temperature T_{irr}. The FC curves then rise and form a dip. Below the dip temperature, the magnetization even exceeds the paramagnetic background above T_c. Interestingly, sample x=0.43 shows a very different behavior. At low field H=0.5 T, one can see a dip. With increasing field, the tip becomes invisible. And ZFC and FC curves show a broad temperature range of reversible magnetization below T_c, which implies a broad vortex liquid regime in the vortex phase diagram. Both the absence of the SMP and the wide reversible magnetization suggest a weak pinning in the sample x=0.43. Salem-Sugui *et al*. had reported the temperature dependence of magnetization at different fields in $(Ba_{1-x}K_x)Fe_2As_2$ (x=0.28 and 0.25) single crystals under ZFC and FC modes

[71]. One may notice that the reversible magnetization below T_c is in a quite narrow temperature window. Most importantly, the FC data always show a dip right below T_c [71]. When one looks over previous results, similar feature was also observed in $BaFe_{2-x}Co_xAs_2$ (x=0.19) [26].

In small size superconductors and ceramic superconductors, a paramagnetic response or paramagnetic Meissner effect (PME) was observed [72]. For small size superconductors, the compression of the flux trapped inside the giant vortex state can result in the PME [73-75]. The PME was also observed in $YBa_2Cu_3O_{7-\delta}$ [76-79] and $La_{1.85}Sr_{0.15}CuO_4$ [80] single crystals. The magnitude of supercurrents flowing in the critical state largely depends on the magnetic fields, temperature, and sample-specific pinning characteristics. One important parameter which also determines the field and current distributions in the FC critical state is the cooling rate. It was demonstrated that one may change the high-field response of the superconductor from diamagnetic to paramagnetic by varying the cooling rate [76-80]. The PME can be understood as the unusual influence of pinning on the FC magnetization caused by the inhomogeneous cooling and subsequent flux compression in a large crystal, mostly due to its size. We have checked the effect of cooling rate on the dip. With applying the fast cooling rate at 20 K/min and slow cooling rate at 1 K/min, we don't find that the dip becomes weak or shifts a lot. It is suggested that the granularity in iron pnictide superconductors close to T_c should be responsible for PME [81]. Keep in mind that the analysis of the vortex interaction energy and pinning force distributions for $Ba(Fe_{1-x}Co_x)_2As_2$ and $BaFe_2(As_{1-x}P_x)_2$ single crystals revealed that the disordered VL should be resulted from strong pinning due to spatial fluctuations of T_c and it is established at a high freezing temperature T_f close to T_c [21-22]. As the sample is cooled down in FC procedure, the screening currents are, at temperatures immediately below T_c, restricted to the intragranular contribution, a situation that remains until the temperature reaches T_{dip}. Below T_{dip},

the intergranular currents might contribute with a signal that can be either paramagnetic or diamagnetic [81].

E. Pinning mechanisms

Our systematic investigations on the magnetization with varying doping x, magnetic field H, temperature T, and time t provide a comprehensive scenario of vortex pinning in $(Ba_{1-x}K_x)Fe_2As_2$ superconductors. The plateau in the double-logarithmic plots of J_c vs H is most pronounced in the sample x=0.26~0.28 and J_c reaches maximum. In $Ba(Fe_{1-x}Co_x)_2As_2$ system, J_c also shows maximum at the boundary where AFM transition line terminates in the phase diagram [10]. The similar feature strongly suggests that the same pinning mechanism should dominate either doping in Ba layers or FeAs layers. A structural phase transition from tetragonal phase to orthorhombic phase is coupled with the AFM transition [48-49]. The formation of structural domains in the orthorhombic phase has been well studied both in $Ba(Fe_{1-x}Co_x)_2As_2$ and $(Ba_{1-x}K_x)Fe_2As_2$ by using polarized light microscopy [10,50-52]. The domain walls extend throughout the samples and act as the extended pinning centers. With the increasing doping x, domain structure becomes more intertwined and fine due to a decrease of the orthorhombic distortion [10], leading to a great enhancement of J_c as doping x approaches ~0.26 in $(Ba_{1-x}K_x)Fe_2As_2$.

We find that the SMP is absent within a narrow doping rnge $0.4<x<0.5$. Furthermore, these samples do not show PME, which implies weak T_c fluctuations. With doping exceeding x=0.51, the SMP reappears. We need to consider another type of pinning center. A quantitative analysis of the T–dependent J_c indicates that the two pinning mechanisms, namely, the spatial variations in T_c (referred to as δT_c pinning) and the fluctuations in the mean free path (δl pinning), are enhanced for the underdoped samples in $(Ba_{1-x}K_x)Fe_2As_2$, which results in the enhancement of J_c [6]. The coexistence of AFM ordered phase and superconducting phase on a scale of dozens of

nanometers was confirmed in a slightly underdoped $(Ba_{1-x}K_x)Fe_2As_2$ single crystal with T_c of 32 K [82]. STM studies reveal nanoscale variations of the local superconducting gap in $BaFe_{1.8}Co_{0.2}As_2$ [23] and $Sr_{0.75}K_{0.25}Fe_2As_2$ [24]. The muon spin rotation (μSR) and infrared spectroscopy experiments demonstrated that bulk magnetism and superconductivity coexist and compete on the nanometer length scale in underdoped $BaFe_{1.89}Co_{0.11}As_2$ [83]. The dopant clusters on the scale of a few nanometers were directly observed in $Ba_{0.72}K_{0.28}Fe_2As_2$ crystals by atom probe tomography technique [84]. It was suggested that the mismatch of dopant size give rise to dopant clustering and electronic inhomogeneity, leading to strong vortex pinning [24]. Unfortunately, TEM measurements can not tell the existence of such dopant clusters. The size of dopant clusters is important, since if they have a dimension significantly less than the coherence length ξ, their effectiveness is reduced by the proximity effect. The formation of dopant clusters gives rise to strong T_c fluctuations, which provides a reasonable explanation for the PME. For the samples x=0.43 and 0.46, we assume the nonexistence of dopant clusters in this doping range, at least a less disordered status compared to the underdoped regime. Recently, the line compounds $CaAFe_4As_4$ (A=K, Rb, Cs) and $SrAFe_4As_4$ (A=Rb, Cs) were found, where alkaline earth metal and alkali metal layers are inserted alternately between the Fe_2As_2 layers along c-axis direction [85]. In $(Ba_{1-x}K_x)Fe_2As_2$ system, the similar line compound $BaKFe_4As_4$ ($Ba_{0.5}K_{0.5}Fe_2As_2$), does not form because of the small differences between their ionic radii [85]. However, the "pseudo line compound" probably forms in $(Ba_{1-x}K_x)Fe_2As_2$ system within the doping range $0.4<x<0.5$. The Ba layers may contain small amount of K atoms, while K layers contain some Ba atoms. Further study needs to be done to clarify this hypothesis.

IV. CONCLUSIONS

We have systematically studied the doping evolution of the shape of the SMP, current

density J_c, magnetization relaxation, PME, microstructures in $(Ba_{1-x}K_x)Fe_2As_2$ superconductors. Our study provides a complete picture for the vortex pinning in $(Ba_{1-x}K_x)Fe_2As_2$ superconductors. We find that J_c reach maximum at x=0.26 at a fixed field H=0.5 T, where AFM transition line terminates in the phase diagram. This feature had been well documented in our previous study on $Ba(Fe_{1-x}Co_x)_2As_2$ system. Two types of pinning sources most probably contribute to the vortex pinning. The domain walls should act as strong pinning centers and greatly enhance J_c in the underdoped regime. On the other hand, the spatial fluctuations of dopant atoms provide a background pinning as point defects ranging from underdoped to overdoped side. With increasing doping x, this background pinning plays a role in the overdoped regime and is responsible for the PE. The SMP disappears in the samples x=0.43 and 0.46. TEM studies showed no obvious difference between the samples with SMP and without SMP. The absence of PME in the samples x=0.43 and 0.46 suggests a small T_c fluctuations and less disordered status. We find that the activation energy U can be described by the logarithmic dependence on critical density J. The three samples x=0.24, 0.32, and 0.43 show the similar magnetic relaxation behavior although the latter does not show the SMP.

ACKNOWLEDGMENTS

This work was supported by the U.S. Department of Energy (DOE), Office of Science, Basic Energy Sciences, Materials Science and Engineering Division. The research was performed at Ames Laboratory, which is operated for the U.S. DOE by Iowa State University under contract # DE-AC02-07CH11358.

References

1. H. Yang, H. Luo, Z. Wang, and H.-H. Wen, Appl. Phys. Lett. **93**, 142506 (2008).
2. H.-J. Kim, Y. Liu, Y. S. Oh, S. Khim, I. Kim, G. R. Stewart, and K. H. Kim, Phys. Rev. B **79**, 014514 (2009).
3. D. L. Sun, Y. Liu, and C. T. Lin, Phys. Rev. B **80**, 144515 (2009).
4. S. Salem-Sugui, Jr., L. Ghivelder, A. D. Alvarenga, L. F. Cohen, K. A. Yates, K. Morrison, J. L. Pimentel, Jr., H. Luo, Z. Wang, and H.-H. Wen, Phys. Rev. B **82**, 054513 (2010).
5. D. Song, S. Ishida, A. Iyo, M. Nakajima, J.-I. Shimoyama, M. Eisterer, and H. Eisaki, Sci. Rep. **6**, 26671 (2016).
6. S. Ishida, D. Song, H. Ogino, A. Iyo, H. Eisaki, M. Nakajima, J.-I. Shimoyama, and M. Eisterer, Phys. Rev. B **95**, 014517 (2017).
7. Y. Nakajima, T. Taen, and T. Tamegai, J. Phys. Soc. Jpn. **78**, 023702 (2009).
8. A. Yamamoto, J. Jaroszynski, C. Tarantini, L. Balicas, J. Jiang, A. Gurevich, D. C. Larbalestier, R. Jin, A. S. Sefat, M. A. McGuire, B. C. Sales, D. K. Christen, and D. Mandrus, Appl. Phys. Lett. **94**, 062511 (2009).
9. R. Prozorov, N. Ni, M. A. Tanatar, V. G. Kogan, R. T. Gordon, C. Martin, E. C. Blomberg, P. Prommapan, J. Q. Yan, S. L. Bud'ko, and P. C. Canfield, Phys. Rev. B **78**, 224506 (2008).
10. R. Prozorov, M. A. Tanatar, N. Ni, A. Kreyssig, S. Nandi, S. L. Bud'ko, A. I. Goldman, and P. C. Canfield, Phys. Rev. B **80**, 174517 (2009).
11. R. Prozorov, M. A. Tanatar, E. C. Blomberg, P. Prommapan, R. T. Gordon, N. Ni, S. L. Bud'ko, and P. C. Canfield, Physica C **469**, 667 (2009).
12. B. Shen, P. Cheng, Z. Wang, L. Fang, C. Ren, L. Shan, and H.-H. Wen, Phys. Rev. B **81**, 014503 (2010).

13. R. Kopeliansky, A. Shaulov, B. Ya. Shapiro, Y. Yeshurun, B. Rosenstein, J. J. Tu, L. J. Li, G. H. Cao, and Z. A. Xu, Phys. Rev. B **81**, 092504 (2010).
14. L. Fang, Y. Jia, J. A. Schlueter, A. Kayani, Z. L. Xiao, H. Claus, U. Welp, A. E. Koshelev, G. W. Crabtree, and W.-K. Kwok, Phys. Rev. B **84**, 140504(R) (2011).
15. S. Salem-Sugui, Jr., J. Mosqueira, A. D. Alvarenga, D. Sóñora, E. P. Herculano, D. Hu, G. Chen, and H. Luo, Supercond. Sci. Technol. **28**, 055017 (2015).
16. L. Ya. Vinnikov, T. M. Artemova, I. S. Veshchunov, N. D. Zhigadlo, J. Karpinski, P. Popovich, D. L. Sun, C. T. Lin, A. V. Boris, JETP Letters **90**, 299 (2009).
17. M. R. Eskildsen, L. Ya. Vinnikov, T. D. Blasius, I. S. Veshchunov, T. M. Artemova, J. M. Densmore, C. D. Dewhurst, N. Ni, A. Kreyssig, S. L. Bud'ko, P. C. Canfield, and A. I. Goldman, Phys. Rev. B **79**, 100501(R) (2009).
18. M. R. Eskildsen, L.Ya. Vinnikov, I. S. Veshchunov, T. M. Artemova, T. D. Blasius, J. M. Densmore, C. D. Dewhurst, N. Ni, A. Kreyssig, S. L. Bud'ko, P. C. Canfield, A. I. Goldman, Physica C **469**, 529 (2009).
19. L. Ya. Vinnikov, A. G. Troshina, I. S. Veschunov, D. Analytis, I. R. Fisher, Y. Liu, C. T. Lin, L. Fang, U. Welp, and W. K. Kwok, JETP Letters **96**, 655 (2013).
20. L. Vinnikov, A. Friedman, I. Felner, A. Troshina, and Y. Yeshurun, J. Phys.: Conf. Ser. **507**, 012013 (2014).
21. S. Demirdiş, C. J. van der Beek, Y. Fasano, N. R. Cejas Bolecek, H. Pastoriza, D. Colson, and F. Rullier-Albenque, Phys. Rev. B **84**, 094517 (2011).
22. S. Demirdiş, Y. Fasano, S. Kasahara, T. Terashima, T. Shibauchi, Y. Matsuda, Marcin Konczykowski, H. Pastoriza, and C. J. van der Beek, Phys. Rev. B **87**, 094506 (2013).
23. Y. Yin, M. Zech, T. L. Williams, X. F. Wang, G. Wu, X. H. Chen, and J. E. Hoffman, Phys.

Rev. Lett. **102**, 097002 (2009).

24. C.-L. Song, Y. Yin, M. Zech, T. Williams, M. M. Yee, G.-F. Chen, J.-L. Luo, N.-L. Wang, E. W. Hudson, and J. E. Hoffman, Phys. Rev. B **87**, 214519 (2013).
25. H. Yang, B. Shen, Z. Wang, L. Shan, C. Ren, and H.-H. Wen, Phys. Rev. B **85**, 014524 (2012).
26. D. S. Inosov, T. Shapoval, V. Neu, U. Wolff, J. S. White, S. Haindl, J. T. Park, D. L. Sun, C. T. Lin, E. M. Forgan, M. S. Viazovska, J. H. Kim, M. Laver, K. Nenkov, O. Khvostikova, S. Kühnemann, and V. Hinkov, Phys. Rev. B **81**, 014513 (2010).
27. P. Das, T. O'Brien, M. Laver, C. D. Dewhurst, N. Ni, S. L. Bud'ko, P. C. Canfield, and M. R. Eskildsen, Supercond. Sci. Technol. **23**, 054007 (2010).
28. L. Shan, Y.-L. Wang, B. Shen, B. Zeng, Y. Huang, A. Li, D. Wang, H. Yang, C. Ren, Q.-H. Wang, S. H. Pan, and H.-H. Wen, Nat. Phys. **7**, 325 (2011).
29. S. Demirdiş, C. J. van der Beek, S. Mühlbauer, Y. Su, and Th Wolf, J. Phys.: Condens. Matter **28**, 425701 (2016).
30. R. Morisaki-Ishii, H. Kawano-Furukawa, A. S. Cameron, L. Lemberger, E. Blackburn, A. T. Holmes, E. M. Forgan, L. M. DeBeer-Schmitt, K. Littrell, M. Nakajima, K. Kihou, C. H. Lee, A. Iyo, H. Eisaki, S. Uchida, J. S. White, C. D. Dewhurst, J. L. Gavilano, and M. Zolliker, Phys. Rev. B **90**, 125116 (2014).
31. H. Kawano-Furukawa, C. J. Bowell, J. S. White, R. W. Heslop, A. S. Cameron, E. M. Forgan, K. Kihou, C. H. Lee, A. Iyo, H. Eisaki, T. Saito, H. Fukazawa, Y. Kohori, R. Cubitt, C. D. Dewhurst, J. L. Gavilano, and M. Zolliker, Phys. Rev. B **84**, 024507 (2011).
32. H. Kawano-Furukawa, Lisa DeBeer-Schmitt, H. Kikuchi, A. S. Cameron, A. T. Holmes, R. W. Heslop, E. M. Forgan, J. S. White, K. Kihou, C. H. Lee, A. Iyo, H. Eisaki, T. Saito, H.

Fukazawa, Y. Kohori, and J. L. Gavilano, Phys. Rev. B **88**, 134524 (2013).

33. X.-L. Wang, S. R. Ghorbani, S.-I. Lee, S. X. Dou, C. T. Lin, T. H. Johansen, K.-H. Müller, Z. X. Cheng, G. Peleckis, M. Shabazi, A. J. Qviller, V. V. Yurchenko, G. L. Sun, and D. L. Sun, Phys. Rev. B **82**, 024525 (2010).
34. C. J. van der Beek, G. Rizza, M. Konczykowski, P. Fertey, I. Monnet, Thierry Klein, R. Okazaki, M. Ishikado, H. Kito, A. Iyo, H. Eisaki, S. Shamoto, M. E. Tillman, S. L. Bud'ko, P. C. Canfield, T. Shibauchi, and Y. Matsuda, Phys. Rev. B **81**, 174517 (2010).
35. C. J. van der Beek, M. Konczykowski, S. Kasahara, T. Terashima, R. Okazaki, T. Shibauchi, and Y. Matsuda, Phys. Rev. Lett. **105**, 267002 (2010).
36. C. J. van der Beek, S. Demirdis, M. Konczykowski, Y. Fasano, N. R. Cejas Bolecek, H. Pastoriza, D. Colson, F. Rullier-Albenque, Physica B: Condensed Matter **407**, 1746 (2012).
37. Y. Liu, M. A. Tanatar, V. G. Kogan, H. Kim, T. A. Lograsso, and R. Prozorov, Phys. Rev. B **87**, 134513 (2013).
38. Y. Liu, M. A. Tanatar, W. E. Straszheim, B. Jensen, K. W. Dennis, R. W. McCallum, V. G. Kogan, R. Prozorov, and T. A. Lograsso, Phys. Rev. B **89**, 134504 (2014).
39. H. Hodovanets, Y. Liu, A. Jesche, S. Ran, E. D. Mun, T. A. Lograsso, S. L. Bud'ko, and Paul C. Canfield, Phys. Rev. B **89**, 224517 (2014).
40. R. Lortz, N. Musolino, Y. Wang, A. Junod, and N. Toyota, Phys. Rev. B **75**, 094503 (2007).
41. A. B. Pippard, Philos. Mag. **19**, 217 (1969).
42. C. P. Bean, Rev. Mod. Phys. **36**, 31 (1964).
43. D. Dew-Hughes, Philos. Mag. **30**, 293 (1974).
44. E. J. Kramer, J. Appl. Phys. **44**, 1360 (1973).
45. A. M. Campbell and J. E. Evetts, Adv. Phys. **21**, 199 (1972).

46. L. Civale, M. W. McElfresh, A. D. Marwick, F. Holtzberg, C. Feild, J. R. Thompson, and D. K. Christen, Phys. Rev. B **43**, 13732(R) (1991).

47. L. Klein, E. R. Yacoby, Y. Yeshurun, A. Erb, G. Müller-Vogt, V. Breit, and H. Wühl, Phys. Rev. B **49**, 4403(R) (1994).

48. M. Rotter, M. Pangerl, M. Tegel, and D. Johrendt, Angew. Chem. Int. Ed. **47**, 7949 (2008).

49. S. Avci, O. Chmaissem, D. Y. Chung, S. Rosenkranz, E. A. Goremychkin, J. P. Castellan, I. S. Todorov, J. A. Schlueter, H. Claus, A. Daoud-Aladine, D. D. Khalyavin, M. G. Kanatzidis, and R. Osborn, Phys. Rev. B **85**, 184507 (2012).

50. M. A. Tanatar, A. Kreyssig, S. Nandi, N. Ni, S. L. Bud'ko, P. C. Canfield, A. I. Goldman, and R. Prozorov, Phys. Rev. B **79**, 180508(R) (2009).

51. E. C. Blomberg, M. A. Tanatar, R. M. Fernandes, I. I. Mazin, Bing Shen, Hai-Hu Wen, M. D. Johannes, J. Schmalian, and R. Prozorov, Nat. Commun. **4**, 1914 (2013).

52. Y. Liu, M. A. Tanatar, E. Timmons, and T. A. Lograsso, Crystals **6**, 142 (2016).

53. C. Ma, H. X. Yang, H. F. Tian, H. L Shi, J. B. Lu, Z. W. Wang, L. J. Zeng, G. F. Chen, N. L. Wang, and J. Q. Li, Phys. Rev. B **79**, 060506(R) (2009).

54. C. Tarantini, S. Lee, F. Kametani, J. Jiang, J. D. Weiss, J. Jaroszynski, C. M. Folkman, E. E. Hellstrom, C. B. Eom, and D. C. Larbalestier, Phys. Rev. B **86**, 214504 (2012).

55. Y. Yeshurun, A. P. Malozemoff, and A. Shaulov, Rev. Mod. Phys. **68**, 911 (1996).

56. Y. Abulafia, A. Shaulov, Y. Wolfus, R. Prozorov, L. Burlachkov, Y. Yeshurun, D. Majer, E. Zeldov, H. Wühl, V. B. Geshkenbein, and V. M. Vinokur, Phys. Rev. Lett. **77**, 1596 (1996).

57. D. Giller, A. Shaulov, R. Prozorov, Y. Abulafia, Y. Wolfus, L. Burlachkov, Y. Yeshurun, E. Zeldov, V. M. Vinokur, J. L. Peng, and R. L. Greene, Phys. Rev. Lett. **79**, 2542 (1997).

58. S. Salem-Sugui, Jr., L. Ghivelder, A. D. Alvarenga, L. F. Cohen, H. Luo, and X. Lu, Phys.

Rev. B **84**, 052510 (2011).

59. G. Blatter, M. V. Feigel'man, V. B. Geshkenbein, A. I. Larkin, and V. M. Vinokur, Rev. Mod. Phys. **66**, 1125 (1994).
60. M. V. Feigel'man, V. B. Geshkenbein, and V. M. Vinokur, Phys. Rev. B **43**, 6263(R) (1991).
61. M. V. Feigel'man, V. B. Geshkenbein, A. I. Larkin, and V. M. Vinokur, Phys. Rev. Lett. **63**, 2303 (1989).
62. A. P. Malozemoff and M. P. A. Fisher, Phys. Rev. B **42**, 6784(R) (1990).
63. D. S. Fisher, M. P. A. Fisher, and D. A. Huse, Phys. Rev. B **43**, 130 (1991).
64. V. M. Vinokur, M. V. Feigel'man, and V. B. Geshkenbein, Phys. Rev. Lett. **67**, 915 (1991).
65. M. P. Maley, J. O. Willis, H. Lessure, and M. E. McHenry. Phys. Rev. B **42**, 2639(R) (1990).
66. M. Konczykowski, C. J. van der Beek, M. A. Tanatar, H. Luo, Z. Wang, B. Shen, H. H. Wen, and R. Prozorov, Phys. Rev. B **86**, 024515 (2012).
67. B. Shen, H. Yang, B. Zeng, C. Ren, X. Xu, H.-H. Wen, arXiv:1111.6105 (unpublished).
68. S. Kokkaliaris, P. A. J. de Groot, S. N. Gordeev, A. A. Zhukov, R. Gagnon, and L. Taillefer, Phys. Rev. Lett. **82**, 5116 (1999).
69. S. Kokkaliaris, A. A. Zhukov, P. A. J. de Groot, R. Gagnon, L. Taillefer, and T. Wolf, Phys. Rev. B **61**, 3655 (2000).
70. D. Giller, A. Shaulov, Y. Yeshurun, and J. Giapintzakis, Phys. Rev. B **60**, 106 (1999).
71. S. Salem-Sugui, Jr., L. Ghivelder, A. D. Alvarenga, J. L. Pimentel, Jr., Huiqian Luo, Zhaosheng Wang, and Hai-Hu Wen, Phys. Rev. B **80**, 014518 (2009).
72. M. S. Li, Physics Reports **376**, 133 (2003).
73. A. K. Geim, S. V. Dubonos, J. G. S. Lok, M. Henini, J. C. Maan, Nature **396**, 144 (1998).
74. A. E. Koshelev and A. I. Larkin, Phys. Rev. B **52**, 13559 (1995).

75. V. V. Moshchalkov, X. G. Qiu, and V. Bruyndoncx, Phys. Rev. B **55**, 11793 (1997).

76. S. Riedling, G. Bräuchle, R. Lucht, K. Röhberg, H. v. Löhneysen, H. Claus, A. Erb, and G. Müller-Vogt, Phys. Rev. B **49**, 13283(R) (1994).

77. R. Lucht, H. v. Löhneysen, H. Claus, M. Kläser, and G. Müller-Vogt, Phys. Rev. B **52**, 9724 (1995).

78. A. A. Zhukov, A. V. Volkozub, and P. A. J. de Groot, Phys. Rev. B **52**, 13013 (1995).

79. A. I. Rykov, S. Tajima, and F. V. Kusmartsev, Phys. Rev. B **55**, 8557 (1997).

80. I. Felner, M. I. Tsindlekht, G. Drachuck, and A. Keren, J. Phys.: Condens. Matter. **25**, 065702 (2013).

81. W. A. C. Passos, P. N. Lisboa-Filho, R. Caparroz, C. C. de Faria, P. C. Venturini, F. M. Araujo-Moreira, S. Sergeenkov, and W. A. Ortiz, Physica C **354**, 189 (2001).

82. J. T. Park, D. S. Inosov, Ch. Niedermayer, G. L. Sun, D. Haug, N. B. Christensen, R. Dinnebier, A. V. Boris, A. J. Drew, L. Schulz, T. Shapoval, U. Wolff, V. Neu, X. Yang, C. T. Lin, B. Keimer, and V. Hinkov, Phys. Rev. Lett. **102**, 117006 (2009).

83. P. Marsik, K. W. Kim, A. Dubroka, M. Rössle, V. K. Malik, L. Schulz, C. N. Wang, Ch. Niedermayer, A. J. Drew, M. Willis, T. Wolf, and C. Bernhard, Phys. Rev. Lett. **105**, 057001 (2010).

84. W. K. Yeoh, B. Gault, X. Y. Cui, C. Zhu, M. P. Moody, L. Li, R. K. Zheng, W. X Li, X. L. Wang, S. X. Dou, G. L. Sun, C. T. Lin, and S. P. Ringer, Phys. Rev. Lett. **106**, 247002 (2011).

85. Akira Iyo, Kenji Kawashima, Tatsuya Kinjo, Taichiro Nishio, Shigeyuki Ishida, Hiroshi Fujihisa, Yoshito Gotoh, Kunihiro Kihou, Hiroshi Eisaki, and Yoshiyuki Yoshida, J. Am. Chem. Soc. 138, 3410 (2016).

Figure captions

FIG. 1. (Color online) Sharp superconducting transition curves and typical magnetization hysteresis loops (MHLs) of $(Ba_{1-x}K_x)Fe_2As_2$ single crystals for selected crystals (a) x=0.18, (b) x=0.38, (c) x=0.43, (d) x=0.57, (e) x=0.70, and (f) x=0.91.

FIG. 2. (Color online) Log-log plots of field dependence of critical current density J_c calculated by the Bean model for the samples (a) x=0.18, (b) x=0.24, (c) x=0.28, (d) x=0.32, (e) x=0.38, (f) x=0.43, (g) x=0.46, (h) x=0.51, (i) x=0.64, (j) x=0.70, (k) x=0.77, and (l) x=0.91. Red dashed lines are guides to the eye.

FIG. 3. (Color online) The normalized pinning force density F_p/F_p^{max} against the reduced field $h = H/H_{irr}$ for the (a) x=0.18, (b) x=0.24, (c) x=0.38, (d) x=0.51, (e) x=0.64, and (f) x=0.70. The arrows indicate the peak position.

FIG. 4. (Color online) (a) The critical current density J_c are extracted at H=0.5 T and plotted as a function of the reduced temperature T/T_c for $(Ba_{1-x}K_x)Fe_2As_2$ crystals. (b) J_c values are further extracted at the different reduced temperatures T/T_c= 0.20, 0.52, and 0.80. The doping dependence of J_c is therefore plotted, which illustrates that J_c reaches maximum at around x=0.26. The arrow indicates a local minimum at x=0.46.

FIG. 5. (Color online) HR-STEM images along (a) [001] and (b) [100] zone axis for the sample x=0.38. Inset of Figure (b) shows the cross section obtained by using FIB. A needle-like second phase is observed in the (100) plane, indicated in the red frame. (c) The view of dislocations in

the TEM image of the sample x=0.38. (d) HR-STEM image along [100] zone axis displays the undulation of the FeAs layers in the sample x=0.46. (e)–(h) Element maps reveal the homogeneous distributions of Ba, K, Fe, and As elements.

FIG. 6. (Color online) (a)-(b) Double-logarithmic plots of time dependence of magnetization at different fields at T=20 K for the sample x=0.24. The red dashed lines are guides to the eye. (c) The MHL at T=20 K shows a SMP at H_{sp}=2.7 T. The empty circles represent the magnetization decay data during a period of 1×10^4 sec. It can be seen that the SMP shifts to $H'_{sp} = 2$ T, indicated by an arrow. The relaxation rate S shows a minimum at S_{min}=1.5 T. Blue solid line is guide to the eye. (d) The plots of $-T\ln|dM/dt|$ against $|M|$, which equals an activation energy U vs J relation. The slope of activation energy U changes at the $H'_{sp} = 2$, which signifies a crossover from elatic to plastic creep.

FIG. 7. (Color online) (a) The decay of magnetization at different temperatures at H=0.5 T for the sample x=0.24. (b) The temperature dependence of relaxation rate S at a fixed field H=0.5 T shows a broad peak at around T=10 K. Solid line is guide to the eye. (c) Semi-logarithmic plot of the temperature dependence of the activation energy U at H=0.5 T. The solid line corresponds to the linear fitting by Eq. (5).

FIG. 8. (Color online) The MHLs together with magnetic relaxation data at (a) T=20 K and (b) T=33 K for the sample x=0.32. The relaxation rate S shows a kink where the MHL has an onset peak. (c) The temperature dependence of relaxation rate S at a fixed field H=0.5 T shows a broad peak at around T=14 K. (d) The temperature dependent U at H=0.5 T fitted by Eq. (5).

FIG. 9. (Color online) Double-logarithmic plots of the time dependence of magnetization (a) at different temperatures at H=0.5 T and (b) at different fields at T=20 K for the sample x=0.43. (c) The MHL together with magnetic relaxation data at T=20 K. (d) The relaxation rate S at H=0.5 T is alomost temperature independent below T=20 K. (l) The temperature dependent U at H=0.5 T is fitted by Eq. (5).

FIG. 10. (Color online) Temperature dependence of magnetization measured in both ZFC and FC procedures for $(Ba_{1-x}K_x)Fe_2As_2$ single crystals; (a) x=0.24, (b) x=0.32, (c) x=0.43, and (d) x=0.64. The arrows indicate the increase of applied magnetic fields. The insets in the Figures show the transition curves in the vicinity of T_c. A dip below T_c, i.e. the PME, is clearly observed in the samples x=0.24, 0.32, and 0.64.

TABLE I. The temperature dependence of the activation energy U for $(Ba_{1-x}K_x)Fe_2As_2$ (x=0.24, 0.32, and 0.43) single crystals is fitted by Eq. (5): $U(J) = U_0 \ln(J_c/J)$. The fitting parameters are summarized in this Table.

K content x	C	U_0	J_c
0.24	40	277.1	7978.8
0.32	40	300.7	13829.4
0.43	36	194.3	6379.3

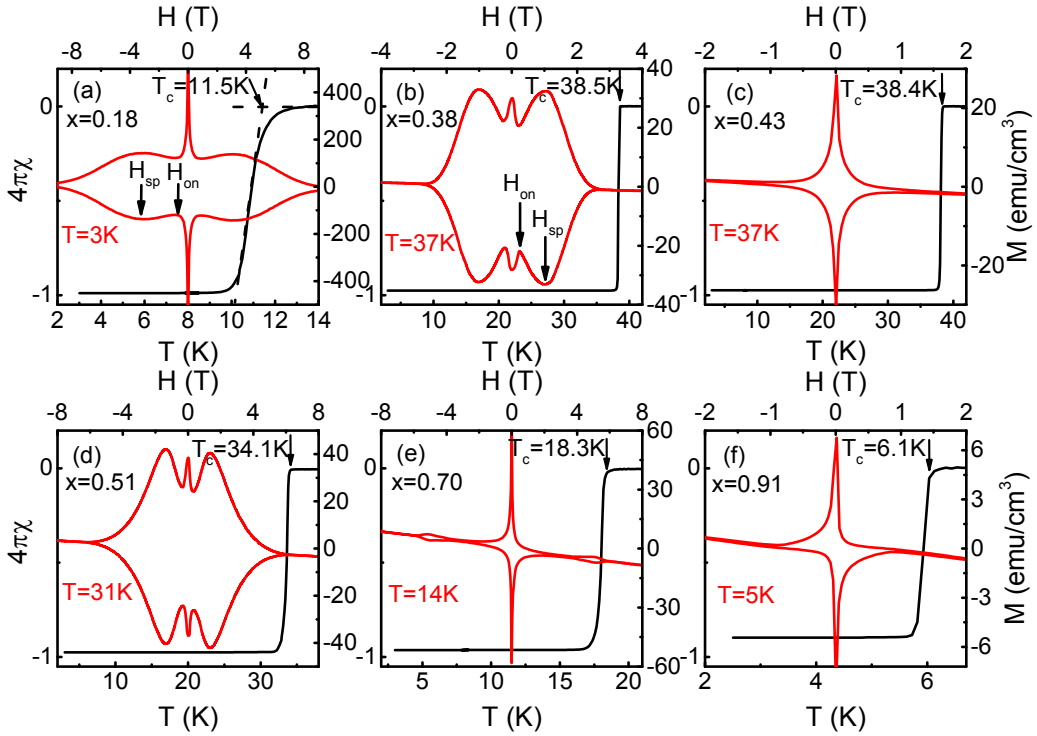
H (T)
(a)
x=0.18
T_c=11.5K
H_sp H_on
T=3K
4πχ
T (K)
(b)
x=0.38
T_c=38.5K
H_on
H_sp
T=37K
(c)
x=0.43
T_c=38.4K
T=37K
M (emu/cm^3)
(d)
x=0.51
T_c=34.1K
T=31K
(e)
x=0.70
T_c=18.3K
T=14K
(f)
x=0.91
T_c=6.1K
T=5K

Figure 1

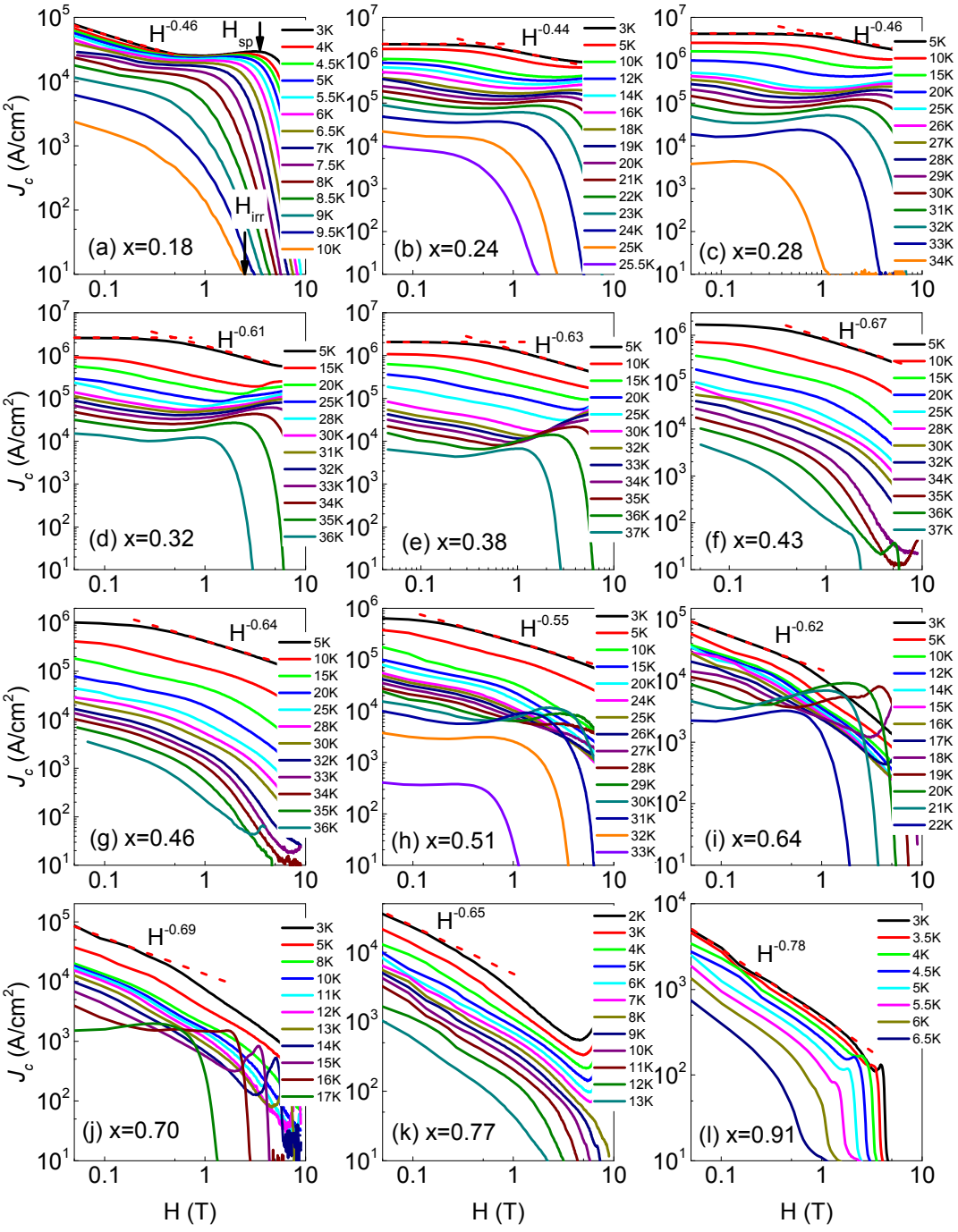
(a) x=0.18
H^-0.46
H_sp
H_irr
3K 4K 4.5K 5K 5.5K 6K 6.5K 7K 7.5K 8K 8.5K 9K 9.5K 10K
(b) x=0.24
H^-0.44
3K 5K 10K 12K 14K 16K 18K 19K 20K 21K 22K 23K 24K 25K 25.5K
(c) x=0.28
H^-0.46
5K 10K 15K 20K 25K 26K 27K 28K 29K 30K 31K 32K 33K 34K
(d) x=0.32
H^-0.61
5K 15K 20K 25K 28K 30K 31K 32K 33K 34K 35K 36K
(e) x=0.38
H^-0.63
5K 10K 15K 20K 25K 30K 32K 33K 34K 35K 36K 37K
(f) x=0.43
H^-0.67
5K 10K 15K 20K 25K 28K 30K 32K 34K 35K 36K 37K
(g) x=0.46
H^-0.64
5K 10K 15K 20K 25K 28K 30K 32K 33K 34K 35K 36K
(h) x=0.51
H^-0.55
3K 5K 10K 15K 20K 24K 25K 26K 27K 28K 29K 30K 31K 32K 33K
(i) x=0.64
H^-0.62
3K 5K 10K 12K 14K 15K 16K 17K 18K 19K 20K 21K 22K
(j) x=0.70
H^-0.69
3K 5K 8K 10K 11K 12K 13K 14K 15K 16K 17K
(k) x=0.77
H^-0.65
2K 3K 4K 5K 6K 7K 8K 9K 10K 11K 12K 13K
(l) x=0.91
H^-0.78
3K 3.5K 4K 4.5K 5K 5.5K 6K 6.5K
J_c (A/cm^2)
H (T)

Figure 2

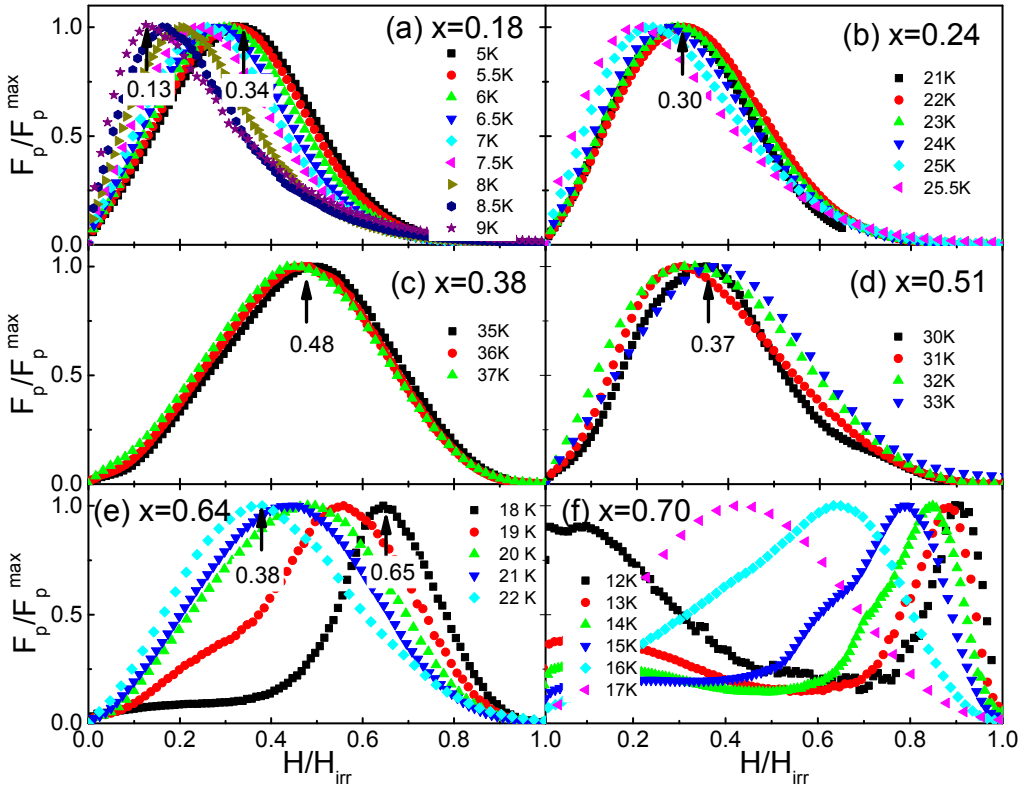
(a) x=0.18
0.13
0.34
5K
5.5K
6K
6.5K
7K
7.5K
8K
8.5K
9K
(b) x=0.24
0.30
21K
22K
23K
24K
25K
25.5K
(c) x=0.38
0.48
35K
36K
37K
(d) x=0.51
0.37
30K
31K
32K
33K
(e) x=0.64
0.38
0.65
18 K
19 K
20 K
21 K
22 K
(f) x=0.70
12K
13K
14K
15K
16K
17K
F_p/F_p^max
H/H_irr

Figure 3

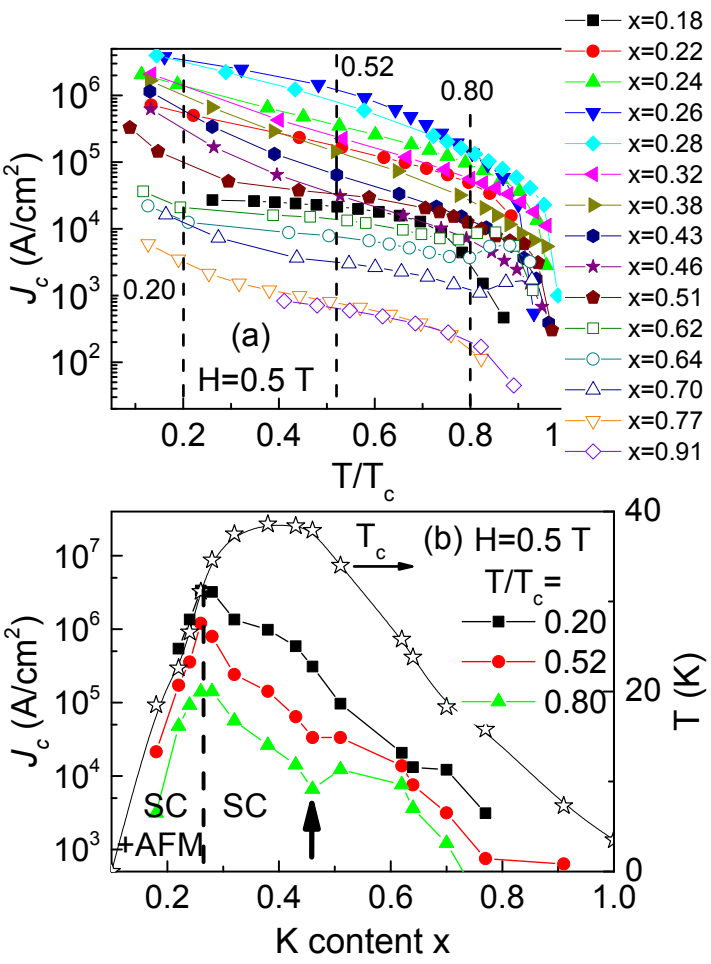
x=0.18
x=0.22
x=0.24
x=0.26
x=0.28
x=0.32
x=0.38
x=0.43
x=0.46
x=0.51
x=0.62
x=0.64
x=0.70
x=0.77
x=0.91
0.52
0.80
0.20
(a)
H=0.5 T
J_c (A/cm^2)
T/T$_c$
(b) H=0.5 T
T$_c$
T/T$_c$ =
0.20
0.52
0.80
SC
+AFM
SC
T (K)
K content x

Figure 4

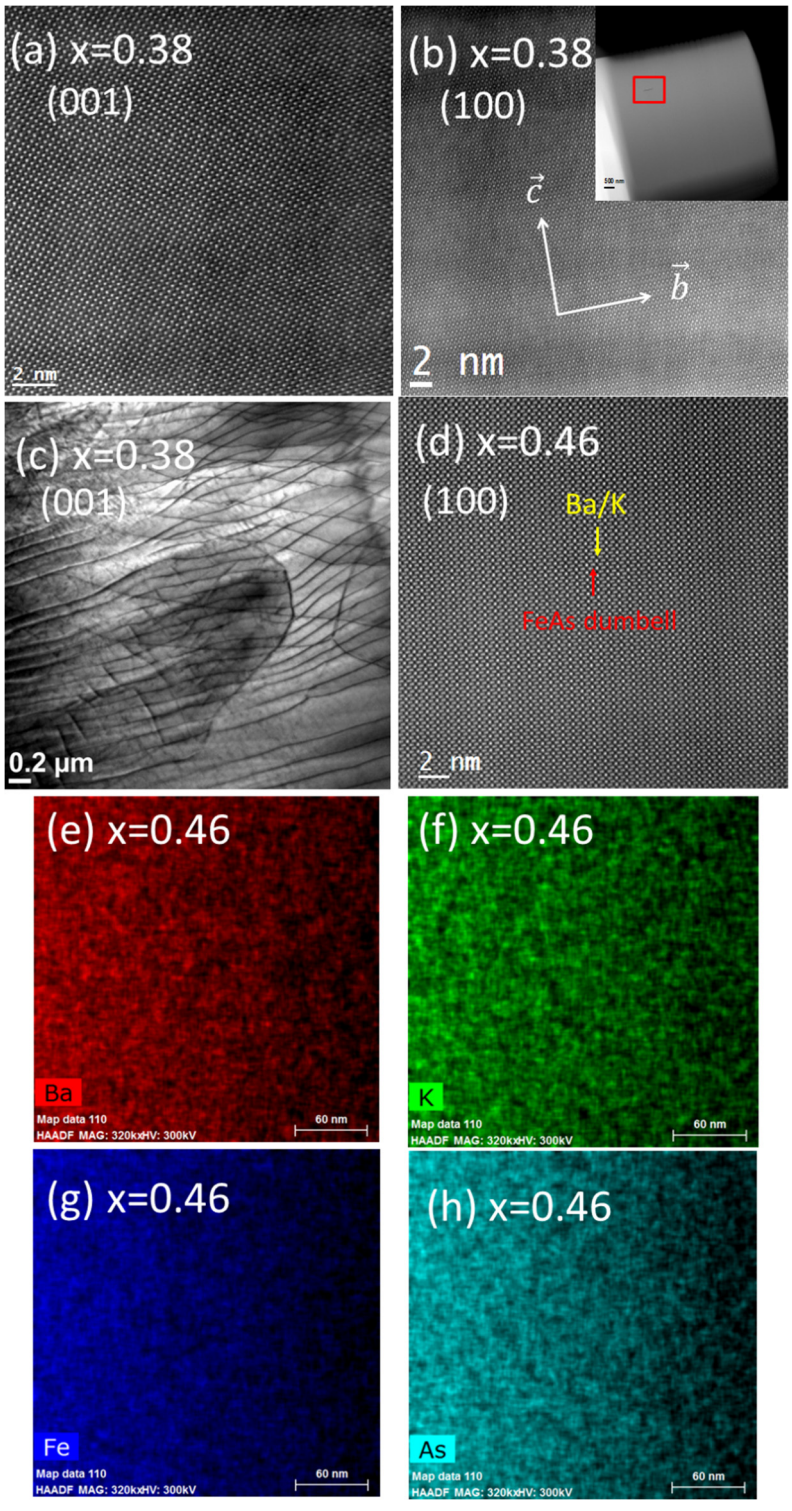
(a) x=0.38
(001)
2 nm
(b) x=0.38
(100)
$\vec{c}$
$\vec{b}$
2 nm
(c) x=0.38
(001)
0.2 μm
(d) x=0.46
(100)
Ba/K
FeAs dumbell
2 nm
(e) x=0.46
Ba
Map data 110
HAADF MAG: 320kxHV: 300kV
60 nm
(f) x=0.46
K
Map data 110
HAADF MAG: 320kxHV: 300kV
60 nm
(g) x=0.46
Fe
Map data 110
HAADF MAG: 320kxHV: 300kV
60 nm
(h) x=0.46
As
Map data 110
HAADF MAG: 320kxHV: 300kV
60 nm

Figure 5

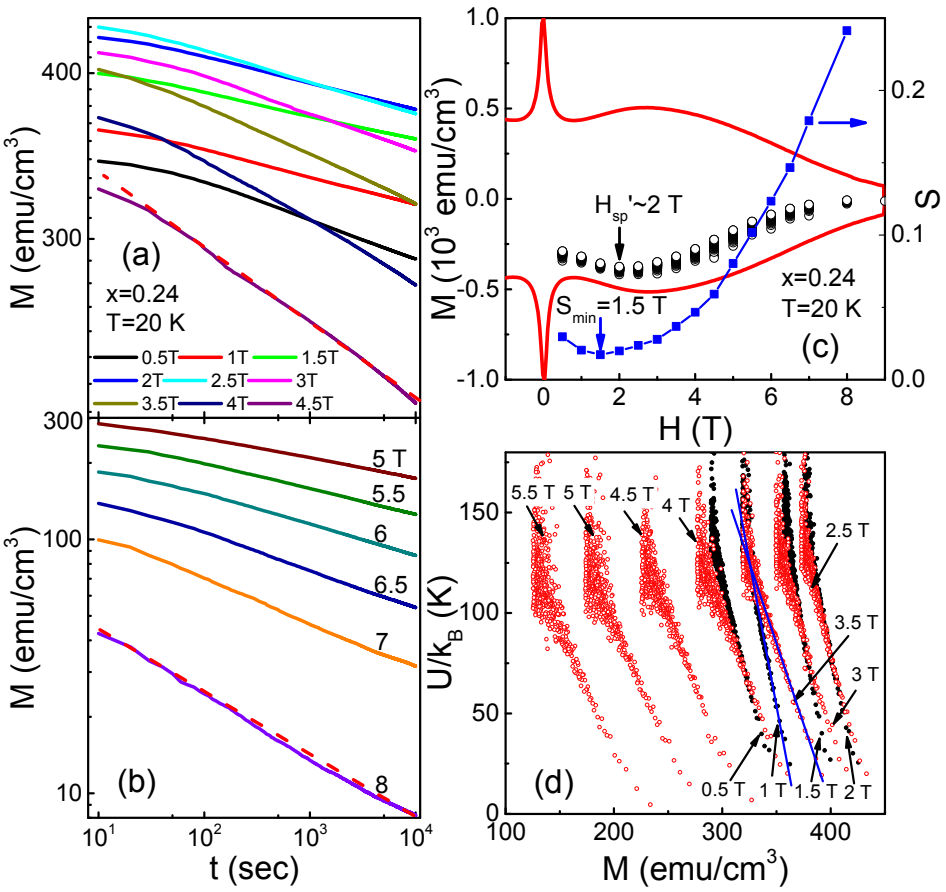
M (emu/cm3)
(a)
x=0.24
T=20 K
0.5T 1T 1.5T
2T 2.5T 3T
3.5T 4T 4.5T
5 T
5.5
6
6.5
7
8
(b)
t (sec)
M (10^3 emu/cm^3)
H_sp'~2 T
S_min=1.5 T
x=0.24
T=20 K
(c)
H (T)
S
U/k_B (K)
5.5 T
5 T
4.5 T
4 T
2.5 T
3.5 T
3 T
0.5 T
1 T
1.5 T
2 T
(d)
M (emu/cm3)

Figure 6

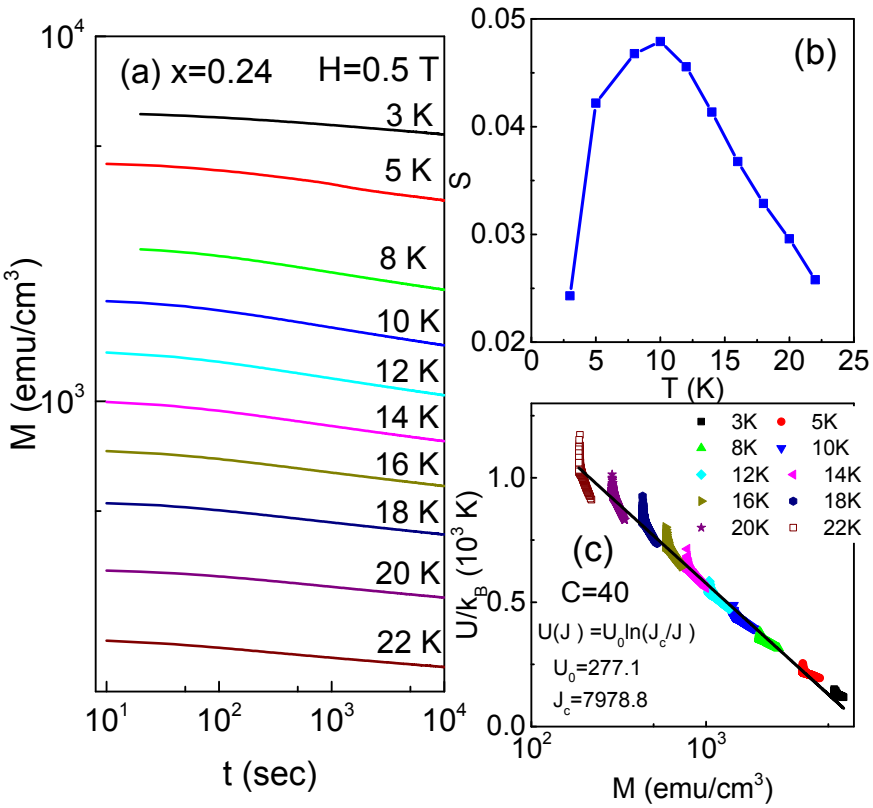
(a) x=0.24 H=0.5 T
3 K
5 K
8 K
10 K
12 K
14 K
16 K
18 K
20 K
22 K
M (emu/cm3)
t (sec)
(b)
S
T (K)
(c)
C=40
U(J) =U0ln(Jc/J)
U0=277.1
Jc=7978.8
U/kB (10^3 K)
M (emu/cm3)

Figure 7

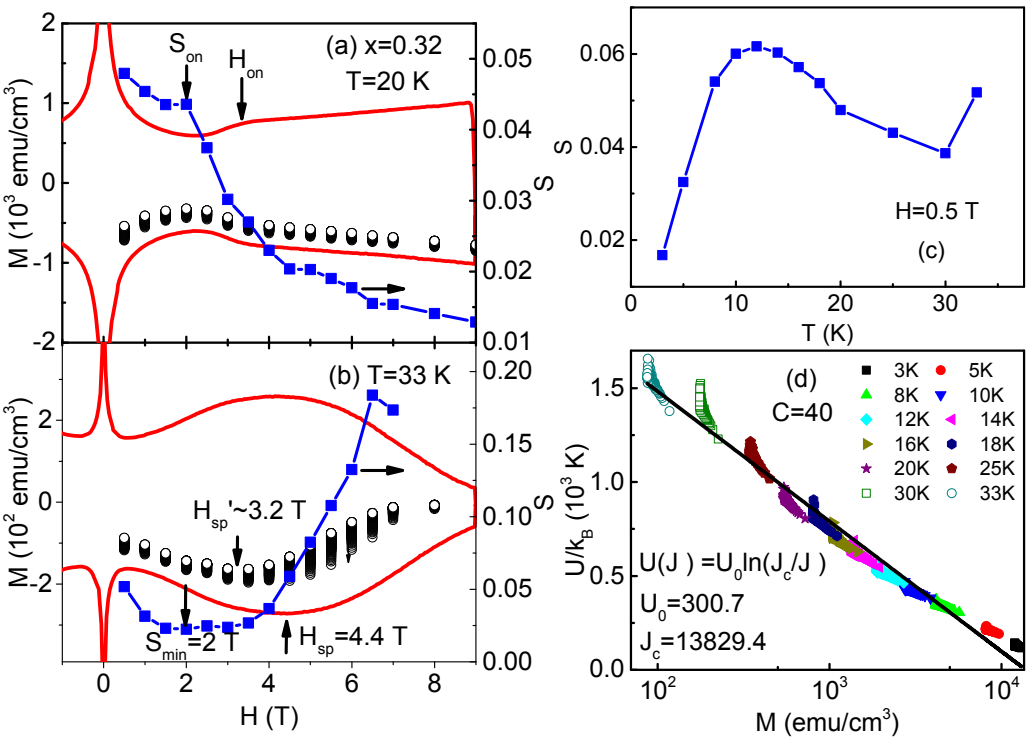
(a) x=0.32
T=20 K
S_on
H_on
M (10^3 emu/cm^3)
S
(b) T=33 K
H_sp'~3.2 T
S_min=2 T
H_sp=4.4 T
M (10^2 emu/cm^3)
H (T)
H=0.5 T
(c)
T (K)
(d)
C=40
3K
5K
8K
10K
12K
14K
16K
18K
20K
25K
30K
33K
U(J) =U_0ln(J_c/J)
U_0=300.7
J_c=13829.4
U/k_B (10^3 K)
M (emu/cm^3)

Figure 8

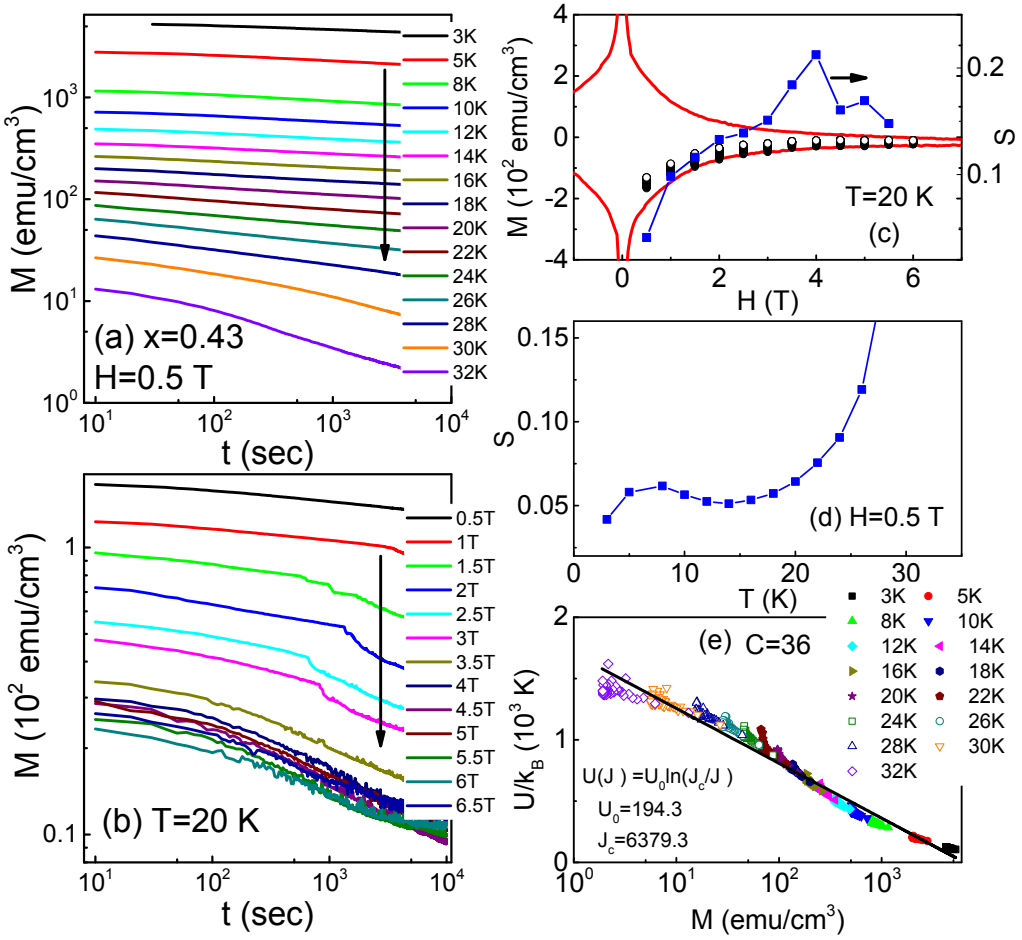
(a) x=0.43
H=0.5 T
M (emu/cm3)
t (sec)
3K
5K
8K
10K
12K
14K
16K
18K
20K
22K
24K
26K
28K
30K
32K
(b) T=20 K
M (10^2 emu/cm^3)
0.5T
1T
1.5T
2T
2.5T
3T
3.5T
4T
4.5T
5T
5.5T
6T
6.5T
T=20 K
(c)
H (T)
S
(d) H=0.5 T
T (K)
(e) C=36
U/k_B (10^3 K)
U(J) =U_0ln(J_c/J)
U_0=194.3
J_c=6379.3
M (emu/cm^3)

Figure 9

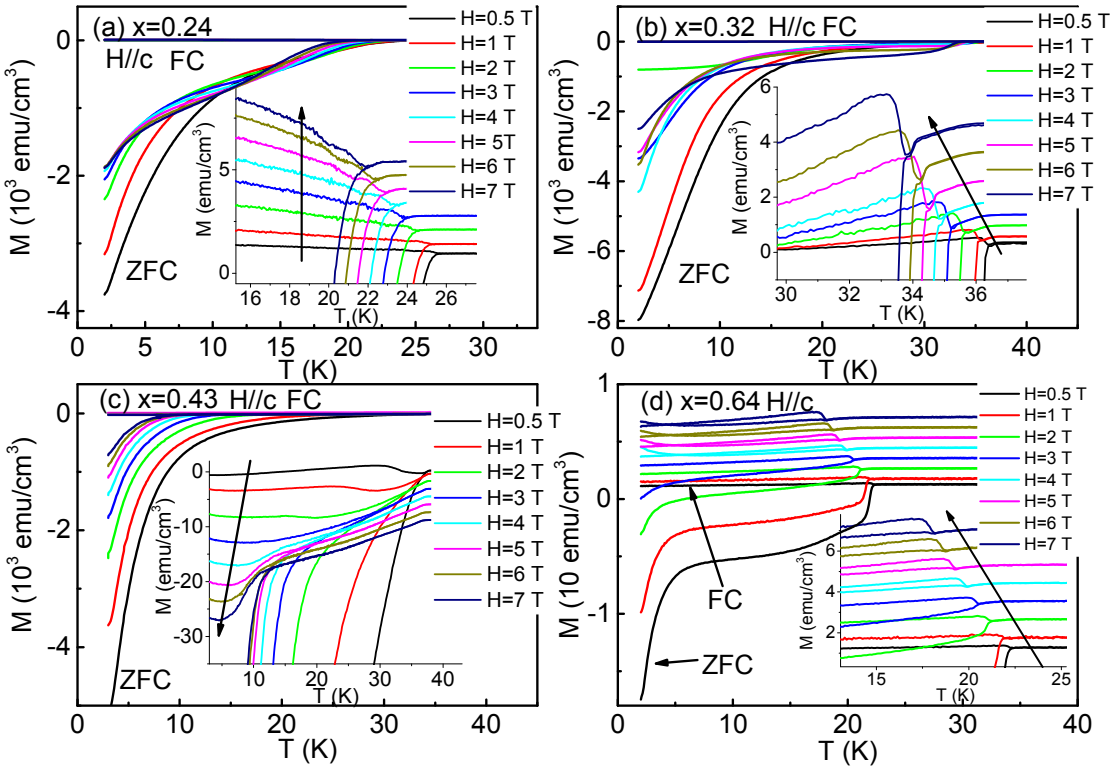
(a) x=0.24
H//c FC
ZFC
H=0.5 T
H=1 T
H=2 T
H=3 T
H=4 T
H= 5T
H=6 T
H=7 T
M (10^3 emu/cm^3)
T (K)
M (emu/cm^3)
T (K)
(b) x=0.32 H//c FC
ZFC
(c) x=0.43 H//c FC
ZFC
(d) x=0.64 H//c
FC
ZFC
M (10 emu/cm^3)

Figure 10